

Definite vacuum for strong-field QED experiments

Qiqi Yu^{1,2,3}, Baifei Shen³, Stefan Bock¹, Ulrich Schramm^{1,4}, Thomas E. Cowan^{1,4}, Roland Sauerbrey^{1,4}, and Hans-Peter Schlenvoigt¹

¹Helmholtz-Zentrum Dresden – Rossendorf, 01328 Dresden, Germany

²Qingdao University of Technology, 266520 Qingdao, People's Republic of China

³Shanghai Normal University, 200234 Shanghai, People's Republic of China

⁴TUD Dresden University of Technology, 01062 Dresden, Germany

Abstract

Ultra-intense lasers can generate the strongest electromagnetic fields in laboratory conditions, expected to perform tests of QED in yet unexplored parameter ranges. Such experiments require knowledge of the field strengths and all possible interaction pathways. The latter can be simplified if a perfect, particle-free vacuum is present, thereby excluding competing interactions. We propose a method to evacuate all residual gas particles prior to QED interactions, based on tunnel ionization by a preceding auxiliary laser pulse and a static electric field. We present modelling and experimental results of testing this method at a 0.5 TW CPA laser system. Experimental results match well the simulations for the given conditions and thereby provide valuable understanding to extrapolate this method to QED experiments with PW-class laser systems where it can likewise be employed for *in-situ* peak field strength characterization.

Keywords: vacuum generation, tunnel ionization, time-of-flight spectroscopy, strong-field QED

1. Introduction

Since the advent of ultra-intense lasers^[1–4], electric/magnetic fields of unprecedented magnitudes are available in laboratories. For laser intensities above 10^{22} W/cm², electric fields exceed 10^{16} V/m where features of radiation reaction, vacuum-polarization, pair production and QED cascades are predicted^[5]. Many proposals have been published for studying the interaction of ultra-intense fields with vacuum^[6–11]. However, the outcome of such planned experiments depends on i) attaining the relevant field strengths in the laser focus and ii) suppressing any background effect which could make the outcome ambiguous. The study of Obst-Huebl *et al.*^[12] highlights how severely laser-generated proton beams can be affected by electric fields from residual gas ionization far off the laser focus. Since strong-field QED experiments require peak intensities of the order of 10^{23} W/cm², residual gas ionization can occur in larger volumes and to high charge states, and therefore must be considered in strong-field QED experiments.

Characterizing the laser focus intensity *in situ* is a challenge and of particular importance for strong-field QED experiments^[13–19]. A widely studied method^[20] relies on the dependency of the attainable ion charge state by tunnel ionization on the laser electric peak field. After ionization

by the short, ultra-intense laser pulse, ions are accelerated in an external static electric field, such that different species are separated temporally due the charge-to-mass-ratio (q/m) dependency of the acceleration, and can be ultimately identified with a time-of-flight (ToF) setup. Recent conceptual studies suggest^[13–16] that this method is reliable for intensities between 10^{20} W/cm² – 10^{24} W/cm².

Other methods to directly infer laser peak intensity, thus avoiding considerable laser-plasma interactions, often utilize electron dynamics and either detect emitted radiation or electron momenta. Ponderomotive scattering of plasma electrons^[21,22] or detection of emitted radiation^[23,24] generally applies to modest peak intensities $< 10^{21}$ W/cm² since electrons are quite light and thus are expelled from peak intensity regions before the laser pulse maximum is reached. Reverting to relativistic electrons (nonlinear Thomson scattering or inverse Compton scattering)^[25,26] ensures that they can stay on laser axis to witness laser peak intensity, but realization is inconvenient due to the need of a well-controlled electron accelerator. An interesting idea^[27] couples tunnel ionization from noble gas atoms, subsequent electron dynamics and radiation emission, and ultimately Breit-Wheeler pair production as chain of processes to infer laser peak intensity. That method is said to be relevant above 10^{23} W/cm², but also highlights the need for a particle-free vacuum as it relies on a QED process.

Correspondence to: hp.schlenvoigt@hzdr.de

We propose to employ the same experimental arrangement of a static electric field as in^[20] in conjunction with an additional, preceding, lower-power fs pulse, to provide a transient particle-free region (void) around the main laser focus, excluding competing effects from residual gas particles^[9]. Thus the same apparatus can be used for both characterizing the main laser pulse (driving the QED experiments) as well as to provide controlled, clean vacuum conditions for QED interactions, allowing for conclusive, unambiguous interpretations.

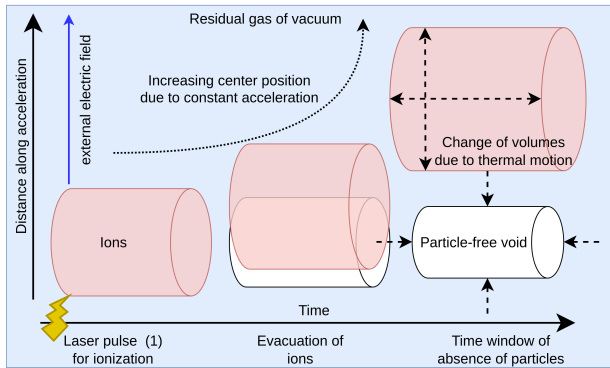


Figure 1: Cartoon of the principle of generating a particle-free, transient void in a vacuum atmosphere. A laser pulse converts all residual gas (blue) within a certain volume into ions (red). A constant, externally applied electric field accelerates the ions in one direction. If that happens fast enough compared to the thermal motion (indicated by dashed arrows), a void (white) can be generated.

The proposed method is depicted in Figure 1. It employs for cleaning a lower-power (few 10 to 100 mJ) and small diameter (few mm) laser pulse to ionize a large region around the main pulse focus. This can be easily achieved with a collinear beam, using the same final focusing optics. Consequently, a large (100 μm) volume of ions (and electrons, not shown) is generated around the location of the main beam focus (few μm). The static external electric field evacuates the charged particles from that region within a time determined by the field strength and region diameter. Then, with a certain delay τ to the first pulse (few 10 ns), the main pulse can arrive in that void and interactions with real particles cannot happen.

Since thermal motion of residual gas and ions is present (indicated by dashed arrows), volumes of void and ions are dynamic. Thermal velocities at room temperature are of the order of 1000 m/s, thus a void of 100 μm size re-fills with residual gas particles on timescales of 100 ns. Eventually, the void vanishes and the average vacuum conditions are recovered.

This concept is relevant for high-power laser QED experiments since typical (thermodynamic equilibrium) vacuum conditions are at the lower end of high vacuum (HV),

10^{-6} mbar or above. The probability to encounter a gas particle per $1 \mu\text{m}^3$ volume is about 1/40 or higher, being much more frequent than the probability for a QED event. Reaching UHV conditions would require bake-out, what will temporarily induce mechanical stress to mounted optics due to different thermal expansion coefficients of optics material (glass) and mounting material (metals). Bake-out would comprise both the experimental chamber as well as the pulse compression chamber, posing a significant risk for pulse compression, beam propagation and alignment.

This article presents a test study of that “cleaning” method. A 0.5 TW CPA laser system was employed, able to achieve intensities up to 10^{16} W/cm². It was modified to generate two pulses with defined delay τ . The second pulse, having a larger beam diameter and more energy than the first pulse, was focused to higher intensities and smaller waist but to the same location as the first one in order to probe whether there were still ions present: If so, it would ionize them to higher charge states than they were already excited by the first pulse, being a clear signature of an interaction of the second pulse with particles in its focus. Ion species distributions were recorded by a ToF detector. For correct pulse timing τ , occurrence of highly charged ions ceased, in agreement with simulations for the experimental parameters.

2. Methods

2.1. Experimental setup

The experiment utilized a 0.5 TW Titanium:Sapphire CPA laser system at 800 nm center wavelength, based on a mode-locked oscillator, grating stretcher, fiber transport to a regenerative amplifier followed by a 6-pass amplifier in free propagation. The amplifiers delivered ca. 25 mJ in a 3 mm diameter beam and s-polarization at 10 Hz repetition rate. The beam diameter was then increased by a Galilei-type 4 \times beam expander to reduce the fluence and provide a better beam propagation.

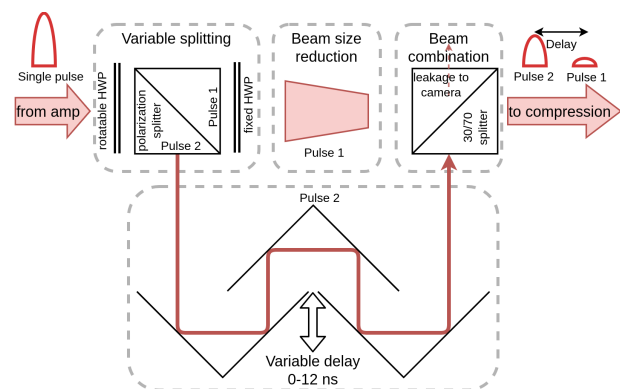


Figure 2: Schematics of the split-and-delay unit (SDU). See the description in the main text.

Then followed a split-and-delay unit (SDU) to create two

pulses with i) variable delay, ii) variable energy ratio and iii) different beam sizes. The schematics of the SDU are shown in Figure 2. A rotatable $\lambda/2$ waveplate combined with a polarization beamsplitter was used to split the laser pulses with arbitrary splitting ratios and without losses. A fixed $\lambda/2$ waveplate was set in the path of the undelayed pulse (pulse 1) to have both pulses in the same polarization. For pulse 2 followed a variable delay path, employing retro-reflector mirrors in 2 passes, allowing for delays up to $\tau = 12$ ns on a 1 m sliding rail. For pulse 1 followed a propagation distance to match the zero delay distance of pulse 2 (not shown) and a beam size reduction by a Galilei-type $2\times$ beam expander in reverse. The beam paths were recombined by a non-polarizing 30 : 70 plate beamsplitter (to sustain the increased fluence in beam 1). It was oriented such that pulse 2 was transmitted with 70% and pulse 1 reflected with 30% relative energy. The parasitic path (70% of pulse 1 and 30% of pulse 2) was used for a nearfield and farfield diagnostic to ensure overlap and collinearity of both beams when changing the delay of pulse 2. The nearfield diagnostic was also employed to find the zero delay position by visible interference fringes. After overlapping, the pulses were sent into a grating pulse compressor (70% transmission).

Laser pulse diagnostics could be inserted into the beam path after laser pulse compression: a Wizzler device to measure and optimize temporal pulse compression; and a laser energy meter to measure pulse energy. Pulse duration was determined to $\tau_{1/2} \approx 55$ fs and was not changed during experiments. Pulse energies were varied by the adjustable waveplate, see above and at subsection 3.1.1.

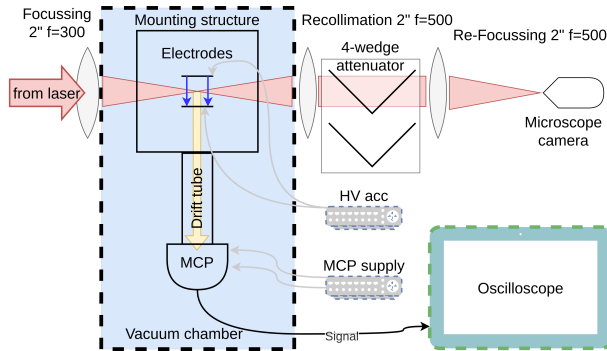


Figure 3: Schematics of the experimental setup. See the description in the main text.

After compression and invasive diagnostics followed ca. 2 m propagation to the interaction chamber, which is shown in Figure 3. The pulses were focused by a $f = 300$ mm achromatic lens into a vacuum chamber with pressure of ca. 7×10^{-7} mbar, achieved by a turbo pump and scroll pump. After passing through the chamber the beams were re-collimated, attenuated by a reflective attenuator assembly and focused again, now in air but below ionization threshold, by $f = 500$ mm achromatic lenses. That provided

a replica of the in-vacuum focus which was finally observed by a camera microscope (Mitutoyo $10\times$ APO and 160 mm tube length). That was a crucial online diagnostic for the spatial overlap of the foci in vacuum, not achievable with the farfield diagnostic before the pulse compression. Focus waists were measured as $w_1 = 40 \mu\text{m}$ and $w_2 = 30 \mu\text{m}$, in reasonable agreement with the beam diameter ratio and absolute beam sizes. Combined with pulse duration and pulse energy, intensities in the range $10^{14} \text{ W/cm}^2 - 10^{16} \text{ W/cm}^2$ were attainable.

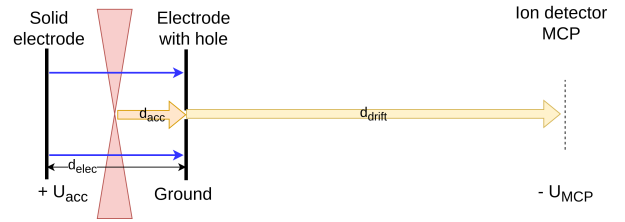


Figure 4: Schematics of the ToF setup. See the description in the main text.

The vacuum chamber housed the electrode assembly, providing the static external electric field (shown in pink) to evacuate the ions out of the focus, and the time-of-flight (ToF) ion detection by means of a micro-channel plate (MCP) detector after a $d_{\text{drift}} = 30$ cm long drift distance for species separation, cf. Figure 4. The electrodes had 20 mm diameter and $d_{\text{elec}} = 4$ mm distance. The left electrode held positive potential U_{acc} , accelerating ions towards the right electrode (on ground). A 1 mm diameter hole in the right electrode allowed for ions from the focus center entering the drift region towards the MCP (on potential $-U_{\text{MCP}}$, slightly accelerating further) but blocked ions from regions of low intensity off center. The Rayleigh lengths for the above-mentioned waists are ≈ 5 mm, thus low-intensity regions are quite long and thus would have generated a large amount of ions of low charge, not relevant for the study. The focus was aligned relative to the hole and in the middle between the electrodes, such that $d_{\text{acc}} \approx 0.5d_{\text{elec}} = 2$ mm. The latter determines the starting position within the electric potential, thus the attainable kinetic energy and hence the ToF time.

For the sections and voltages as depicted in Figure 4, the ToF time may be calculated as given by Eq. 1, where amu is the atomic mass unit, e_0 the elementary charge, A the ion's mass number and Z its charge.

$$T_{\text{ToF}} = \sqrt{\frac{2 \text{ amu}}{e_0}} \sqrt{\frac{A}{Z}} \times \left[\sqrt{\frac{d_{\text{acc}}}{U_{\text{acc}}/d_{\text{elec}}}} + \sqrt{\frac{U_{\text{acc}} d_{\text{acc}} d_{\text{drift}}^2}{U_{\text{MCP}}^2 d_{\text{elec}}} \left(\sqrt{1 + \frac{U_{\text{MCP}} d_{\text{elec}}}{U_{\text{acc}} d_{\text{acc}}} - 1} \right)} \right] \quad (1)$$

One can show that the fastest species with $A/Z = 1$, being

hydrogen ions, take several hundred nanoseconds. Molecule ions from species in air can have $A/Z \sim 30$ and therefore take up to ca. 6 times longer, on the microsecond scale. Thus, ion detection requires a time resolution of about 100 ns (at a full range of about $10 \mu\text{s}$) in order to discriminate the ion species. To further identify which of the pulses generated certain ions, 1 ns time resolution would be required, what was not available. Thus the pulse identification must be done by differential measurements of pulse 1 only, pulse 2 only and pulse 1&2 combined in order to reveal the void generation by absence of particles for the second pulse at specific conditions.

2.2. Experiment design

For preparation and detailed design of the experiment, two simulation suites were developed: One modeled quantitatively the ionization of residual gas by a focused and pulsed Gaussian beam in 3D, providing charge state probability density distributions. A second one modeled the evolution of initially cylindrical volumes of ideal gas, as shown in Figure 1, under the action of an external electric field and finite temperature, and computed the number of particles in a second cylindrical volume as function of time.

The first simulation modeled the focus laser intensity distribution in space and time $I(x, y, z, t)$ as product of a purely spatial and a purely temporal dependency, such as

$$I(x, y, z, t) = I_0 \times \mathcal{I}(r, z) \times \tilde{I}(t) \quad (2)$$

The spatial dependency was modeled as Gaussian beam $\mathcal{I}(r, z)$ in cylindrical symmetry coordinates $r = \sqrt{x^2 + y^2}$, z where the longitudinal coordinate z is the beam propagation axis. It took as input the laser pulse wavelength λ , Gaussian beam waist before focusing w_{beam} and the focal length f , such as

$$\mathcal{I}(r, z) = \frac{1}{1 + z^2/z_R^2} \exp\left(-2\frac{r^2}{w^2(z)}\right) \quad (3a)$$

$$w(z) = w_0 \sqrt{1 + z^2/z_R^2} \quad (3b)$$

$$z_R = \pi w_0^2/\lambda \quad (3c)$$

$$w_0 = \lambda f/(\pi w_{\text{beam}}) \quad (3d)$$

The temporal dependency $\tilde{I}(t)$ was modeled as Gaussian pulse, characterized by a FWHM pulse duration $\tau_{1/2}$, such as

$$\tilde{I}(t) = \exp((\ln 0.5)t^2/\tau_{1/2}^2) \quad (4)$$

All shape functions were maximum-normalized, such that a single factor I_0 , the peak intensity in focus $r = z = 0$ and at temporal maximum $t = 0$, could be employed. To relate I_0 to the pulse energy W_L , integration over space and time was employed.

In a second step, the generation of ions from the residual gas species (N_2 , O_2 , H_2O) was computed by the numerical modelling^[28] of tunnel ionization^[29,30] included in PICongPU^[31] (not the full PIC suite), using the respective ionization potentials of molecular and atomic ions from NIST^[32] and employing both the temporal intensity envelope $\tilde{I}(t)$ and the peak intensity I_0 for linear polarization. For the remainder, we consider only the resulting ionization (after the laser pulse is over) and introduce the local peak intensity

$$\hat{I}(r, z) = I_0 \times \mathcal{I}(r, z) \quad (5)$$

A result from this step for $\lambda = 800 \text{ nm}$ and $\tau_{1/2} = 55 \text{ fs}$ is shown in Figure 5. It displays the probability for ion species (different charge states) from nitrogen and oxygen, N^{1+} , N^{2+} , etc. and O^{1+} , O^{2+} etc., dependent on laser peak intensity. These ions are relevant for this study since they can be altered by the second, more intense pulse by further ionization to a charge state higher than the first pulse can produce. Ionized molecules such as N_2^+ , O_2^+ , H_2O^+ can occur at low intensities as well but will Coulomb-explode when being ionized further. Hydrogen ions H^+ cannot be altered.

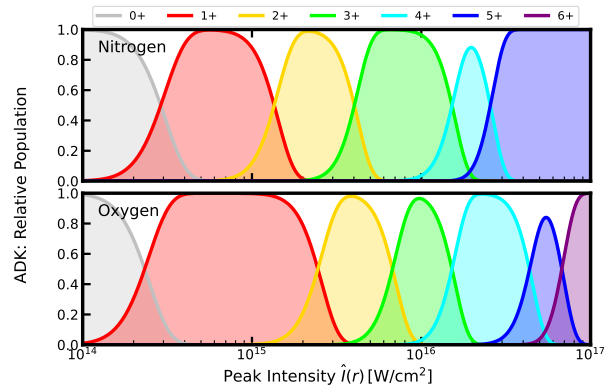


Figure 5: Model dependency of generated ion species from nitrogen and oxygen on laser peak intensity for a 55 fs Gaussian laser pulse, at the end of the laser pulse. Oxygen exhibits a relative long interval of O^+ until further electrons become ionized.

Figure 5 shows a first mandatory condition: Any pulse must exceed a threshold intensity

$$I_{\text{Thr}} = 5 \times 10^{14} \text{ W/cm}^2 \quad (6)$$

in order to ionize any gas particle. Here, nitrogen sets the limit to achieve a high probability for N^{1+} ; O^{1+} is already at $4 \times 10^{14} \text{ W/cm}^2$ certainly ionized. This threshold intensity ensures that all gas molecules are ionized and can then be evacuated by the external electric field.

Secondly, Figure 5 also shows that for any peak intensity of pulse 1, pulse 2 must be a factor 5 more intense in order

to ionize particles to a higher charge state than pulse 1, and thereby mark them as detected. Here, the value is given by oxygen in order to ionize O^{1+} from pulse 1 to O^{2+} by pulse 2. This leads to a second condition

$$\hat{I}^{P2}(r, z) > 5 \times \hat{I}^{P1}(r, z) \quad (7)$$

ensuring that species, generated by pulse 1, can be modified by pulse 2 if they are still present upon arrival of pulse 2, in order to discriminate ions from pulse 1 and pulse 2.

Mapping the peak-intensity-dependent ion species probabilities to the local peak intensity $\hat{I}(r, z)$ given by the spatial intensity modelling (Eq. 3), the simulation could compute for given experimental laser parameters the species-resolved probability densities in 3D, which can be sampled on points, lines, planes or summed over volumes.

That was done, as second design refinement, perpendicular to the beam direction, first at $z = 0$. Figure 6 shows for

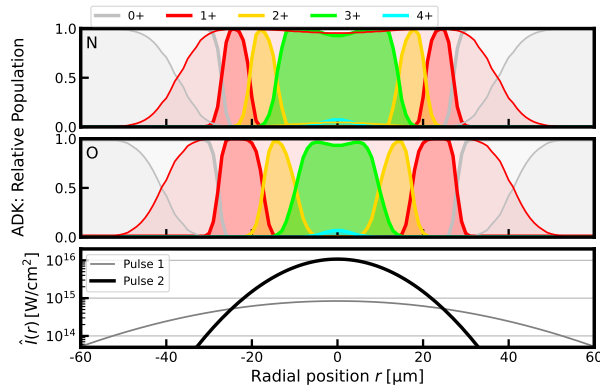


Figure 6: Simulated radial ion species distribution in focus ($z = 0$) for an ideal case: Pulse 1 is focused to $50 \mu\text{m}$ waist with 2 mJ, yielding $8.4 \times 10^{14} \text{ W/cm}^2$ peak intensity; pulse 2 is focused to $20 \mu\text{m}$ waist with 4 mJ, yielding $1.1 \times 10^{16} \text{ W/cm}^2$ peak intensity. The radial intensity profiles are shown in the bottom panel, pulse 1 as thin gray line and pulse 2 as thick black line. Above are the radial ion species distributions for nitrogen (top panel) and oxygen (center panel). Thin lines represent distributions after pulse 1, thick lines after pulse 2.

an idealized case (see caption) the radial ion distributions generated by pulse 1 (thin) and pulse 2 (thick), respectively.

Concerning condition Eq. 6, pulse 1 ionizes the residual gas to single-charged ions N^{1+} and O^{1+} but not higher (thin lines in upper panels). Due to the spatial dependency given by Eq. 5, a cleaning radius R_{clean} can be defined by inserting Eq. 5 into Eq. 6 and solving for r . It can be found for the example of Figure 6

$$R_{\text{clean}} \approx 30 \mu\text{m} \quad (8)$$

Pulse 2, on the other hand, is able to generate single-, double-

and triple-charged ions. Hence a pulse 2 only signal would be very different from a pulse 1 only signal. Furthermore, ion generation by pulse 2 is restricted to a region fully contained within the region of single-charged ions from pulse 1; pulse 2 is unable to generate any ions outside the distribution from pulse 1, $r > 30 \mu\text{m}$. Consequently, if the single-charged ions generated by pulse 1 are evacuated by the external electric field upon arrival of pulse 2 (evacuation not part of this simulation suite but other, see later), the region $0 < r < 30 \mu\text{m}$ will contain no particles. Hence pulse 2 cannot generate any ions in addition to those generated earlier by pulse 1, and a pulse 1&2 combined ion signal would be identical to a pulse 1 only signal, being evidence of the generation of the void.

However, if particles are still present, condition Eq. 7 must be considered, which can be generalized, depending on the ion species of pulse 1 and pulse 2: A probing radius R_{probe} can be defined where pulse 2 could generate ion species nowhere accessible with pulse 1, given by the corresponding, species-dependent threshold intensity, yielding $R_{\text{probe}}(X^{n+})$ for species X in charge state n .

In order to be able to alter ions from pulse 1 for probing but also to probe only within the cleaning region, a third condition must be fulfilled which reads as

$$0 < R_{\text{probe}}(X^{n+}) < R_{\text{clean}} \quad (9)$$

For actual experiments with limited alignment accuracy of both beams, this translates to an alignment margin

$$\Delta r(X^{n+}) = R_{\text{clean}} - R_{\text{probe}}(X^{n+}) \quad (10)$$

This margin depends not only on the general focus shapes and intensities but also on the ion species under investigation.

Table 1 summarizes the respective radii from the example of Figure 6. Choosing highly-charged ions as detection channel implies a smaller region where these ions can be generated. This provides a larger alignment margin but comes at the cost of a smaller number of ions possibly generated.

Species	R_{clean}	R_{probe}	Δr
N^{1+}	$28 \mu\text{m}$	–	–
N^{2+}	–	$18 \mu\text{m}$	$10 \mu\text{m}$
N^{3+}	–	$13 \mu\text{m}$	$15 \mu\text{m}$
O^{1+}	$30 \mu\text{m}$	–	–
O^{2+}	–	$15 \mu\text{m}$	$15 \mu\text{m}$
O^{3+}	–	$8 \mu\text{m}$	$22 \mu\text{m}$

Table 1: Radii from Figure 6 where pulse 1 can generate N^{1+} or O^{1+} (being R_{clean}) and where pulse 2 can generate higher charge states (being R_{probe}), and the respective differences as defined by Eq. 9.

In the experimental realization, such ideal laser diameter conditions as discussed above could not be obtained. The waist ratio was rather 40:30 instead of 50:20, and pulse energies could not be varied independently. Most critical was that the area where pulse 2 generated the same (single-charged) species as pulse 1 was not contained within that area of pulse 1. The results for such more realistic case are shown in Figure 7. As can be seen, the waist ratio is

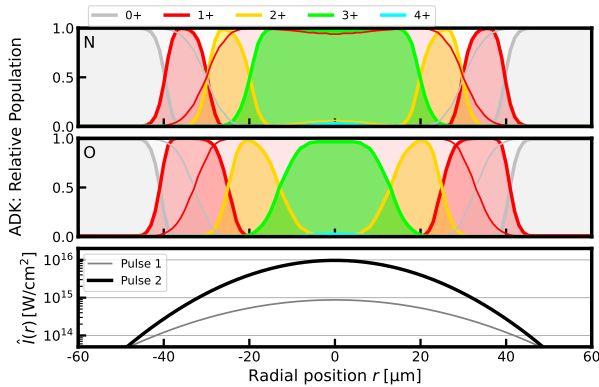


Figure 7: Simulated radial ion species distribution as in Figure 6 but for realistic conditions. Pulse 1 is focused to $40\ \mu\text{m}$ waist with $1.3\ \text{mJ}$, yielding $8.8 \times 10^{14}\ \text{W}/\text{cm}^2$ peak intensity; pulse 2 is focused to $30\ \mu\text{m}$ waist with $8\ \text{mJ}$, yielding $9.7 \times 10^{15}\ \text{W}/\text{cm}^2$ peak intensity.

insufficient to prevent that pulse 2 generates N^{1+} and O^{1+} ions outside where pulse 1 does so. Thus, pulse 2 will always generate those ions by ionizing residual gas, left over from pulse 1, in addition to these species generated by pulse 1. Still, N^{3+} and O^{3+} are exclusive to pulse 2, and their absence in a pulse 1&2 combined ion signal would indicate absence of particles and thus the generation of the void. While that is qualitatively the same as for the ideal case, the radial margin between the region of highest charged ions from pulse 2 and ionization by pulse 1 has reduced from ca. $20\ \mu\text{m}$ for the ideal case to ca. $10\ \mu\text{m}$ for the realistic case. This quantitative change turned out to be very critical during realization.

Figure 8 shows the radial distributions as in Figure 7 but out of focus for different positions along the beam axis. This is important because pulse 1 and pulse 2 evolve differently along z , pulse 2 will eventually obtain a larger diameter in any case (also for the ideal case) and thus it will not be contained within pulse 1.

The experimental setup included a $1\ \text{mm}$ diameter aperture for the ions. Thereby, only ions generated within $|z| \leq 500\ \mu\text{m}$ were detected. The distribution for that limit $z = 500\ \mu\text{m}$ is shown in the upper graph of Figure 8. There are only negligible differences to the in-focus case $z = 0$, Figure 7. The bottom graph of Figure 8 shows the distributions at $z = 2\ \text{mm}$, being quantitatively different from $z = 0$ and thereby demonstrating the importance of

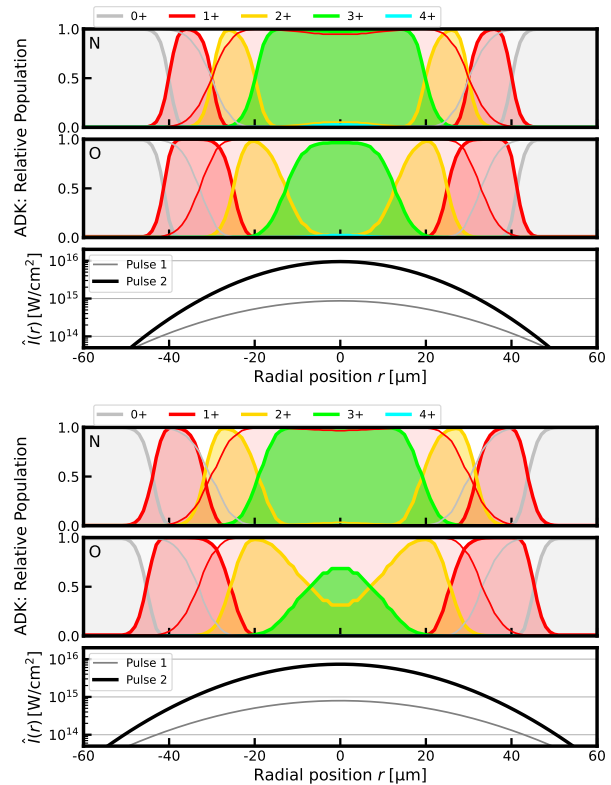


Figure 8: Simulated radial ion species distribution as in Figure 7 but out of focus at $z = 500\ \mu\text{m}$ (top) and $z = 2\ \text{mm}$ (bottom).

the aperture.

The second simulation suite was used to study the trade-off between cleaning and probing radii, external field strength and pulse delay τ . It models two cylindrical volumes like in Figure 1: One for the ions generated by pulse 1 (with R_{clean}), and a second one where pulse 2 can generate the highest charge states (with R_{probe}). That is a fair approximation as the previous paragraphs have shown: species probabilities vary steeply in radial direction and very weak in longitudinal direction. The simulation models the time-dependence of the particle probability density for i) an initially cylindrical low-Z ion distribution under the influence of both an external electric field and thermal motion, and ii) for the remaining volume of residual gas (inverse cylinder) with thermal motion only, cf. Figure 1. Coulomb repulsion of ions is not considered. It yields, as function of time, the number of particles (either ions or neutral molecules) expected to be found inside the second cylindrical volume of length $L_{\text{probe}} = 1\ \text{mm}$ (and $L_{\text{clean}} \gg L_{\text{probe}}$), representing the region where pulse 2 can generate specific ions. The radii, temperature, particle masses, charge state and electric field play a role.

Figure 9 displays the simulation results for low and high acceleration voltage and for further parameters as described

earlier ($d_{\text{elec}} = 4 \text{ mm}$, $R_{\text{clean}} = 30 \mu\text{m}$ and $R_{\text{probe}} = 20 \mu\text{m}$). It shows the particle numbers of single-charged ($Z = 1$) atomic or molecular ions created by pulse 1 within the volume where pulse 2 could generate higher charge states, relative to the source molecule density.

For a few nanoseconds, there is no change of number because the volume where particles are counted is smaller than the original volume of particles. Please note the factor 2 for atomic ions which originate from di-atomic gas molecules. Then, after a time of a few ns, the numbers decrease, faster with higher acceleration voltage. This is the result of the evacuation of ions due to the external electric field. Separations by ion masses are visible. At late times in the shown time window, a slight increase is visible as result of thermal motion of the residual gas molecules, filling up the void, what leads to a temperature dependence. In the experiment, delays up to $\tau = 12 \text{ ns}$ were available, requiring voltages of at least 1 kV according to this simulation.

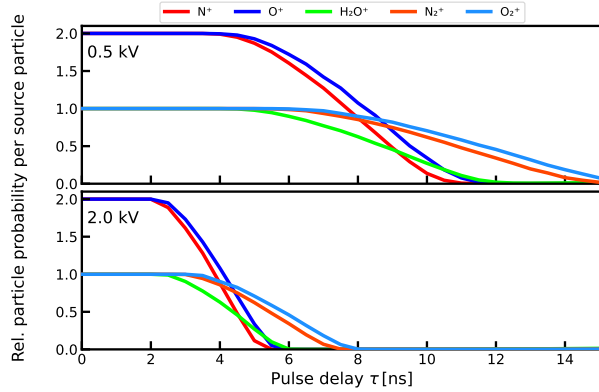


Figure 9: (Simulation) Time dependence of low- Z ions, generated by pulse 1 and accelerated transversely by the static electric field (low and high voltage), counted within the probing volume relative to the initial number of gas molecules. Volume dimensions are as in Figure 6, $R_{\text{clean}} = 30 \mu\text{m}$ and $R_{\text{probe}} = 20 \mu\text{m}$.

A further information from the second simulation suite is the absolute number of particles, since it took not only the temperature to derive the mean particle velocity but also the pressure to infer actual numbers instead of probabilities.

The number of ions depends on the pulse ionization volume $V = \pi R^2 L$ with L being the cylinder length, vacuum pressure p , n_0 the particle density per unit pressure (e.g. $n_0 \approx 2.5 \times 10^4 \mu\text{m}^{-3}/\text{mbar}$), q the relative contribution of the source species to the residual gas, and M how many ions can be generated from a source species (e.g. $M = 2$ for N^{n+} from N_2), and is given by

$$N = Mqn_0pV \quad (11)$$

For a pressure of 10^{-6} mbar and a length of 1 mm (limited

by the aperture in the electrode), about 7×10^4 gas particles can be ionized by pulse 1 with $R_{\text{clean}} = 30 \mu\text{m}$. Pulse 2 should certainly dissociate any original particles ($M=2$) and thus still generate 6×10^4 ions for $R_{\text{probe}} = 20 \mu\text{m}$.

3. Results

3.1. Setup characterization

3.1.1. Optical setup Key for ion detection (and their absence) is proper adjustment of the laser pulses in terms of their respective spatial intensity distributions Eq. 5 and their mutual overlap, Eq. 10. For intensity characterization, pulse energy, pulse duration and focus relay imaging were combined.

Pulse energies were varied in a coupled manner by the variable waveplate before the beam splitting (see Figure 2). We used 4 different settings (10° , 15° , 20° , 25°), changing both pulse 1 and pulse 2 energies. For pulse 1 only and pulse 2 only, focus intensity distribution analysis was done (using pulse energy W_L and pulse duration $\tau_{1/2}$), yielding peak intensity value, FWHM and $1/e^2$ areas. Results are listed in Table 2. The waveplate angle determined mainly pulse energies, and to minor extent also the apparent focus waists. With increasing waveplate angle, the energy of pulse 1 was increasing whereas the energy of pulse 2 was decreasing. The range of settings ensured that pulse 1 was always intense enough to generate ions at all (cf. Eq. 6, condition 1), and pulse 2 was always more intense than pulse 1 by a factor 3 – 20 (cf. Eq. 7, condition 2). In fact, that condition was not satisfied for 25° waveplate angle.

3.1.2. ToF ion detection Investigations started with single pulse operation, either pulse 1 only or pulse 2 only. Figure 10 shows the time-resolved MCP ion detector signal as a composite graph of pulse 1 (low intensity, purple) and pulse 2 (high intensity, orange) for 15° waveplate angle. Ion species appear as signal peaks at specific times but are followed by some electrical ringing.

Most important for analysis was the assignment of ion charge states to the peaks, since the simulations made clear that only specific high charge states can be employed to witness the formation of a void. This assignment was realized by the dependence of ToF times to specific charge-to-mass ratios A/Z , cf. Eq. 1, with $T_{\text{ToF}} \propto \sqrt{A/Z}$. Thus, plotting (not shown) each peak's ToF time versus $\sqrt{A/Z}$ for educated guesses of the ion mass A and charge state Z helped to identify the species, starting here from the slowest, as molecular ions O_2^{1+} , N_2^{1+} and H_2O^{1+} , followed then by atomic ions (listed here by charge state): $\text{O}^{1+} \dots \text{O}^{3+}$, $\text{N}^{1+} \dots \text{N}^{3+}$ and H^+ as fastest species. These are shown as labels in Figure 10 and are already first results, essential for further analysis. Also the experiment time offset relative to the external trigger was found this way by extrapolating $T_{\text{ToF}}(\sqrt{A/Z})$ for $A/Z = 0$.

Quantity	Waveplate angle			
	10°	15°	20°	25°
w_0^{P1}	31.8 μm	32.7 μm	35.5 μm	39.2 μm
W_L^{P1}	0.6 mJ	1.3 mJ	2.3 mJ	3.2 mJ
I_0^{P1}	6×10^{14} W/cm ²	1.3×10^{15} W/cm ²	1.9×10^{15} W/cm ²	2.2×10^{15} W/cm ²
w_0^{P2}	29.2 μm	28.0 μm	26.4 μm	27.6 μm
W_L^{P2}	9.3 mJ	8.2 mJ	6.6 mJ	4.6 mJ
I_0^{P2}	1.3×10^{16} W/cm ²	1.2×10^{16} W/cm ²	1.1×10^{16} W/cm ²	7×10^{15} W/cm ²
ratio of W_L	1 : 15	1 : 6.3	1 : 2.9	1 : 1.4
ratio of I_0	1 : 22	1 : 10	1 : 5.5	1 : 3.2

Table 2: Results of pulse energy measurements and focus analysis for the 4 employed waveplate settings and either pulse 1 or pulse 2, here for $\tau = 3$ ns optical delay path. Data for other delays is similar.

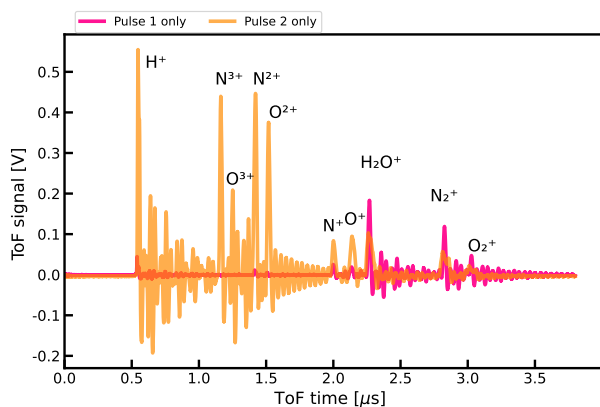


Figure 10: Measured Time-of-Flight ion detector traces for pulse 1 only and pulse 2 only, effectively two different laser intensities. The waveplate was set to 15°, thus the energy ratio was 1:6, the peak intensity ratio ca. 1:10; the voltage was $U_{\text{acc}} = 2$ kV.

Further analysis used only the detector peak voltages, no ion numbers were inferred. Already peak height reading was limited by the detector's ringing. If specific peaks might have vanished completely, the ringing may have been mistakenly read as non-zero peak height, thereby underestimating the cleaning.

Laser conditions for Figure 10 are listed in Table 2 for 15° and are close to those of Figure 7. The experimentally observed ion species agree well with predictions based on focus analysis, the peak intensity allows for ionization and dissociation of nitrogen and oxygen molecules and to ionize the fragments mainly to the first charge state, only in the center to the second charge state ions. Pulse 2, in contrast, was set to 9× higher intensities in order to ionize the atoms or ions further up to $Z = 3$, exactly what we observed. In addition, the peaks for $Z > 1$ are stronger than those for $Z = 1$, showing the stronger MCP response for ions with higher Z . In turn, that implies the the number of $Z = 2$ ions from pulse 1 is indeed very small. Essentially, the conditions

are chosen such that $Z = 3$ ions are exclusive to pulse 2, being one crucial condition to test the void generation.

3.1.3. Spatial overlap A second requirement for void detection is the overlap of the intensity regions for cleaning and probing in space. That overlap was set by manually adjustable mirror mounts before the beam recombination of the SDU (see Figure 2). After setting the overlap, data was taken immediately to avoid drifts of the overlap. Detail overlap analysis was done after taking all data and revealed that the necessarily strong peak intensity discrepancy, up to 20×, limited the precision of overlapping the peak positions during alignment (even with live image processing) and often, the actual peak distance exceeded the margins. We refrained from altering the beam path by e.g. using neutral density filters for pulse 2, in order to not alter thereby the apparent position on the camera, what would lead to misalignment.

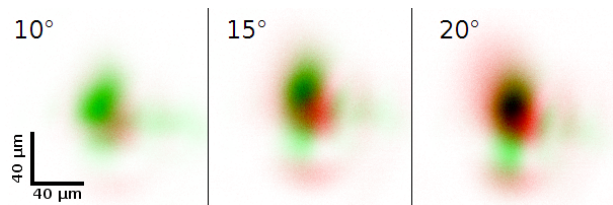


Figure 11: Series of focus composite images for the given waveplate angles (measurement). Each composite is of same scale and shows the focus of beam 1 in red, that of beam 2 in green. At good overlap and for similar intensities, the colors mix (inversely) to black. Data from $\tau = 9$ ns optical delay.

Figure 11 shows composite focus images for 3 different waveplate settings. In each panel, the focus of beam 1 is colored red, the one of beam 2 in green, and they mix to black. For 10° waveplate angle, beam 1 is barely visible but located to the lower right of beam 2. This is also true for the other two cases, but for 20° it is also visible top-left of beam 2. That means that beam 1 stretches over beam 2. Yet, the beams have always the same relative location, only their

appearance is changed, demonstrating the difficulty to assess the overlap.

However, as it was discussed earlier, margins are specific to peak intensity conditions. Table 2 shows that for 10° waveplate angle, pulse 2 is most intense and could generate highest charge states, but pulse 1 is so weak that the area of cleaning is relatively small, limiting *per se* the alignment margin Δr . With increasing angle, the cleaned region grows and the regions for a specific charge state as witness shrink, thus enhancing the alignment margin. On the other hand, too small probing volumes for a specific charge state imply that the possible number of witness ions is very small, and could be masked by the detector's ringing.

The detailed analysis processed the areal measures of focus analysis to infer a mean focus radial measure, either as HWHM or waist, assuming circular symmetry. With those measures and the peak intensities, relevant radii R_{clean} and $R_{\text{probe}}(X^{n+})$ were inferred in order to calculate the allowable alignment margin Δr according to Eq. 10. The intensity peak positions were used to calculate the actual alignment offset. A comparison with the allowable margin provided then information, whether cleaning should be detectable (actual peak distance less than Δr) or not, helping to select the right data sets.

Table 3 shows actual mean radii and alignment margins for the 4 waveplate settings. R_{clean} is determined by $I^{P1} = 3 \times 10^{14} \text{ W/cm}^2$ (condition 1), slightly lower than in Eq. 6, R_{probe} is determined by $I^{P2} = 5 \times 10^{15} \text{ W/cm}^2$ in order to generate N^{3+} , fulfilling Eq. 7 (condition 2). Δr is given by Eq. 10 and checks for condition 3 (Eq. 9). Table 3 shows that the setting of 10° is not very promising since the cleaned region is too small and pulse 2 will always (even for perfect alignment) encounter neutral residual gas and ionize it into the highest charge state, such that no complete disappearance of ions in this state can be ever detected. Conversely, the largest waveplate angle of 25° provides ample alignment margin, but the area to generate highest charge states is quite small and thus the possible number of ions is ca. $4 \times$ lower ($A \propto R^2$) than for 10° . Furthermore, the cleaning pulse was intense enough to generate $Z = 2$ ions.

Waveplate	R_{clean}	R_{probe}	Δr
10°	$12.3 \mu\text{m}$	$13.3 \mu\text{m}$	$-1.0 \mu\text{m}$
15°	$17.9 \mu\text{m}$	$12.2 \mu\text{m}$	$5.7 \mu\text{m}$
20°	$22.1 \mu\text{m}$	$10.4 \mu\text{m}$	$11.8 \mu\text{m}$
25°	$25.5 \mu\text{m}$	$6.5 \mu\text{m}$	$19.0 \mu\text{m}$

Table 3: Overview of experimentally realized radii for cleaning volumes and probing volumes. R_{clean} is determined by $I = 3 \times 10^{14} \text{ W/cm}^2$, slightly lower than in Eq. 6, R_{probe} is determined by $I = 5 \times 10^{15} \text{ W/cm}^2$ in order to generate N^{3+} , fulfilling Eq. 7. Δr is given by Eq. 10 and checks for condition Eq. 9.

Eq. 11 allows to calculate the possible number of ions generated with pulse 2. Here we use $p = 7 \times 10^{-6} \text{ mbar}$ pressure, $L = 1 \text{ mm}$ (given by the hole in the electrode) and the respective values of R_{probe} , furthermore $M = 2$ and $q = 1$ for an upper limit estimate. For 10° , up to 2×10^4 ions could be generated, for 25° only 4.6×10^3 .

3.2. Void generation measurement

Measurements for void generation and detection were taken for various parameters. Most central was the variation of the delay between pulse 1 and pulse 2, where 5 settings were realized: $\tau \in \{0; 3; 6; 9; 12\} \text{ ns}$. Secondly, 4 different waveplate orientations were chosen ($\{10; 15; 20; 25\}^\circ$), providing 4 different energy ratios and thus 4 different peak intensities, as mentioned before. Thereby differently wide cleaning regions were realized at the cost of possibly little number of potential witness ions. Furthermore, 4 different acceleration voltages were employed, $U_{\text{acc}} \in \{0.5; 1.0; 1.5; 2.0\} \text{ kV}$. That was done to possibly reduce the electrical ringing for peak identification. Finally, for each setting, traces of pulse 1 only, pulse 2 only and pulse 1&2 combined were recorded, summing up to 240 measurements where ToF traces and focus relay images were taken simultaneously. Analysis of spatial overlap showed that the overlap for $\tau = 12 \text{ ns}$ was not well established, thus limiting the potential for void detection at that particular delay.

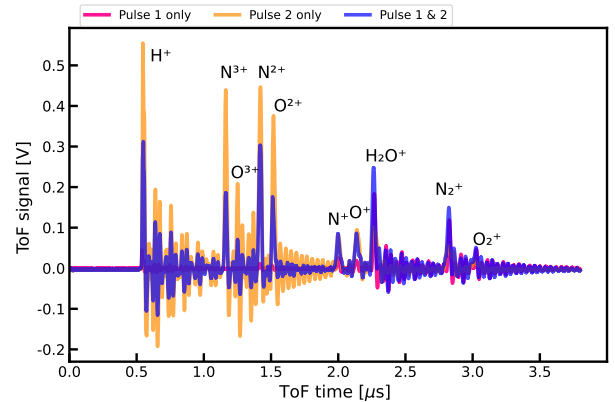


Figure 12: Measured ion signal ToF traces for the same conditions as Figure 10, here also with the trace when both pulses were shot with $\tau = 9 \text{ ns}$. As can be seen, numbers of species H^+ , N^{3+} , O^{3+} , N^{2+} and O^{2+} are reduced by ca. 40 – 60%.

An example ToF ion detector trace for void generation is shown in Figure 12. It displays the same data as Figure 10 (pink, orange) but with the additional trace (blue) when both pulses were fired with $\tau = 9 \text{ ns}$ delay. For that case, the number of species H^+ , N^{3+} , O^{3+} , N^{2+} , O^{2+} is reduced (blue) compared to the case of pulse 2 only (orange). That means that pulse 2 encountered less oxygen

or nitrogen ions when pulse 1 was shot $\tau = 9$ ns earlier, because those species were already moving out of the focus region of pulse 2. The number of species N^{1+} and O^{1+} is mainly unchanged, since these species cannot witness the void formation. The number of molecular ions H_2O^{1+} , N_2^{1+} and O_2^{1+} is slightly increased. These are generated at the outer areas of the focus from neutral residual gas, which moves back into the void after these species were generated by pulse 1, thus pulse 2 can generate some more of these species, in particular at longer delays.

For further analysis, ToF traces were processed to determine for each species the peak height. Let H_1 , H_2 and H_3 be the signal amplitude for pulse 1 only, pulse 2 only and pulse 1&2 combined, respectively, for a given species. Then, the relative height change was computed when both pulses were fired, relative to the height for pulse 2 only, as

$$\Delta = \frac{H_3 - H_2}{H_2} \quad (12)$$

If the ion peak for pulse 1&2 combined vanishes, $H_3 \equiv 0$, there would be 100% reduction, $\Delta = -100\%$.

Now, the relative reduction Δ for specific species as function of pulse delay τ can be visualized for further parameters like acceleration voltage or waveplate setting. Figure 13 shows the relative reduction of detected species versus delay τ for fastest acceleration $U_{\text{acc}} = 2$ kV. Several features can be recognized.

First, the waveplate angle determines the transverse size of the cleaned region. For 10° , this region is relatively small because the peak intensity of pulse 1 is low. On the other hand, pulse 2 is very intense and can generate species, which are in principle able to witness the cleaning, at regions where pulse 1 was too weak and consequently, neutral residual gas is present which is not affected by the electric field. Therefore the variation of species number due to cleaning is weak, limited to 40%. Furthermore, a relatively small void can be faster re-filled with residual gas. This may explain the comeback to $\Delta = 0$ at delays larger than 6 ns.

Conversely, at 25° , the cleaned region is large and cleaning is best at the longest delay. On the other hand, the probing pulse has weakest intensity and the possible number of highly charged ions is small. In fact, O^{3+} was almost never observed except for $\tau = 3$ ns where a single data point exists.

For the other waveplate configurations, conditions were between these extreme cases. Reduction of species can be observed for delays in a consistent way and was stronger than for 10° , up to 75%.

It must be noted that the traces are coded by detected species, not the evacuated species like in a simulation, cf. Figure 9. For some of the detected species, several source species are possible. For example, N^{3+} can be generated by pulse 2 from N^{2+} , N^{1+} or N_2^{1+} , depending on the actual peak intensity of pulse 1. Yet, evacuation of all these different source species by the external electric

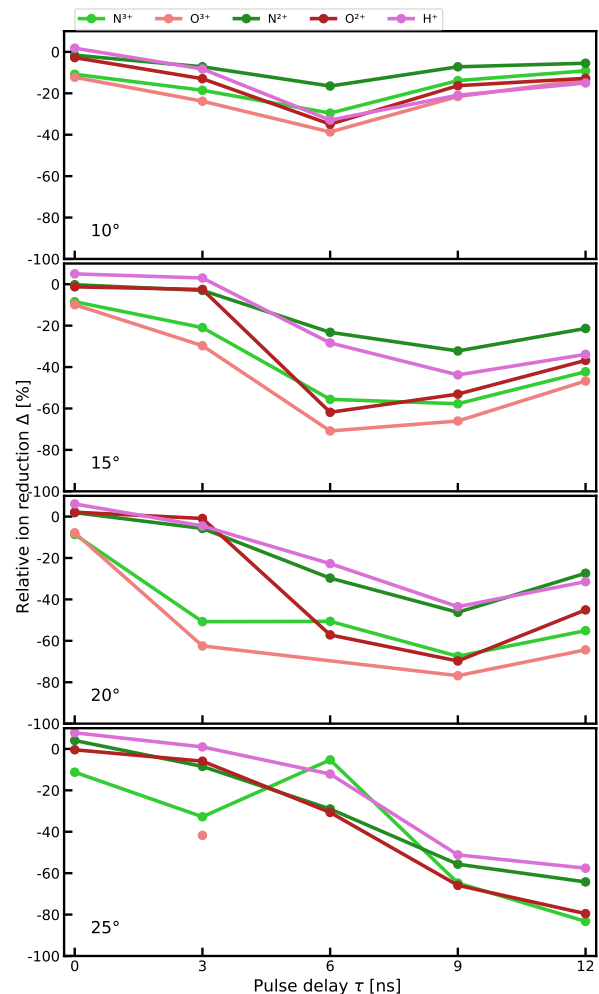


Figure 13: Relative change of peak height versus optical pulse delay τ , for the 4 waveplate settings and for high acceleration voltage (measurement).

field happens with different timescales due to different A/Z . Opposite to that case is H^+ which can only originate from H_2O^{1+} .

In the panel for 20° of Figure 13, we observe that the evacuation detected by N^{3+} and O^{3+} (light green and light pink) is faster than for the other displayed species. This can be explained as follows: N^{3+} as detected species shows the average evacuation of N^{2+} , N^{1+} and N_2^{1+} , where N^{2+} leaves faster than the others. By contrast, N^{2+} as detected species shows the average evacuation of N^{1+} and N_2^{1+} , what is the same as for the former case except the $Z = 2$ ions.

In summary, void generation was demonstrated but not to 100% reduction, given by limitations in terms of maximum delay τ , focus diameters (determined ultimately by available laser pulse energy) and focus overlap accuracy.

4. Outlook

4.1. Cleaning at QED experiments

Based on the successful demonstration of vacuum cleaning under limited conditions, an experiment for realistic conditions can be planned. We assume here that a QED experiment will employ a PW-scale short-pulse CPA laser to provide the strong background field. To initiate the cleaning process, we suggest that the preceding cleaning pulse is sent along the same path, utilizing the same focusing optics and thereby minimizing the setup and alignment needs. The cleaning pulse must have a smaller beam diameter (hence longer F-number) in order to obtain a focus much larger than the main beam. We further fix the incoming beam fluence (intensity) to the same value as the QED drive pulse, typically the highest reasonable value below damage thresholds of optics, thus carrying the most energy per beam size unit. In the simplest case, the cleaning pulse could be a portion of the main beam, taking a short-cut path in order to arrive earlier.

Table 4 shows an example for a 800 nm (Ti:Sapphire) QED drive laser beam of 2 PW nominal power. The beam size is chosen conservatively (large) to lower the beam fluence and intensity to 50 mJ/cm² and 2×10^{12} W/cm², respectively. A flat-top beam profile is assumed. An effective beam waist of 1/4th of the beam diameter allows to employ Gaussian beam focusing (Eq. 3) to derive the in-focus parameters.

The three right columns of Table 4 show the corresponding quantities for a cleaning beam as function of the relative fraction in beam diameter $\eta = D_{\text{clean}}/D_{\text{QED}} < 1$. By fixing the beam fluence and pulse duration, the cleaning beam has a factor η^2 of the main pulse energy, a spot size $1/\eta$ and a peak intensity η^4 of the QED beam. For a QED beam

reaching 10^{22} W/cm² and the cleaning beam to exceed 5×10^{14} W/cm² (cf. Eq. 6), η must be of the order of a few percent. This ensures that the QED drive beam is almost unchanged when picking a small fraction for the cleaning process. In general, a smaller η provides a larger beam waist of the cleaning pulse, but it also reduces the pulse energy. The example lists for illustration that a beam with $\eta = 1\%$ is insufficient for cleaning because its peak intensity does not reach the threshold intensity given by Eq. 6, whereas larger fractions can be employed for cleaning.

We take for further modelling $R_{\text{probe}} = w_0 = 2 \mu\text{m}$ and $L_{\text{probe}} = 2z_{\text{R}} = 32 \mu\text{m}$ from the QED beam and for the cleaning pulse the values for $\eta = 2\%$, $R_{\text{clean}} = 90 \mu\text{m}$ and $L_{\text{clean}} = R_{\text{clean}}$ to reduce computation efforts.

Another prerequisite is detailed knowledge about the residual gas composition since the void formation must be achieved with high reliability. Assuming that the vacuum chamber has negligible outgassing and diffusion through seals, the residual gas composition is mainly given by the ambient atmosphere via gas backstreaming. Such composition is listed in Table 5. Heavy ions are limiting the evacuation process since they take the longest time. This is in our case Argon and carbon dioxide. For partial recovery of the average vacuum conditions by thermal motion, the lightest species are important, here Helium.

Based on the geometry parameters, simulations of the evacuation and recovery process can be done, showing a time window when a particle-free vacuum is present at the probe volume. Since the simulations model the particles with a Maxwellian velocity distribution, they yield an expectation value for the number of particles within a volume.

Here, the earlier described method was only employed for evacuation. For recovery of the average vacuum conditions at later times, computational efforts of that method became

Quantity	QED beam	Cleaning beam		
Cleaning fraction η		1,00 %	2,00 %	5,00 %
Beam diameter D	350 mm	3.5 mm	7 mm	17.5 mm
Energy W_L	50 J	5 mJ	20 mJ	120 mJ
Pulse duration	25 fs		same as QED beam	
Beam power P_L	2 PW	200 GW	800 GW	5 TW
Beam fluence	52 mJ/cm ²		same as QED beam	
Beam intensity	2×10^{12} W/cm ²		same as QED beam	
Effective waist w_{beam}	88 mm	0.88 mm	1.8 mm	4.4 mm
Beam Rayleigh length $z_{\text{R,beam}}$	30 km	3 m	12 m	75 m
F-number	F/2	F/200	F/100	F/40
Focus waist w_0	2 μm	200 μm	100 μm	40 μm
Focus Rayleigh length z_{R}	16 μm	160 mm	41 mm	6.5 mm
Focus peak intensity I_0	10^{22} W/cm ² †	1.5×10^{14} W/cm ²	2.5×10^{15} W/cm ²	1×10^{17} W/cm ²
Cleaning radius R_{clean}	6.2 μm	–	91 μm	66 μm

Table 4: Quantities of the QED drive beam and for the cleaning beam, as function of a radial fraction of the main beam. Both have 800 nm central wavelength.

†: Assuming 65% of the energy contained within the focus of the QED beam.

Contribution	Mass in a.m.u.	rel. amounts
Nitrogen	28	7.73×10^{-1}
Oxygen	32	2.07×10^{-1}
Water	18	9.90×10^{-3}
Argon	40	9.25×10^{-3}
Carbon dioxide	44	4.13×10^{-4}
Neon	20	1.80×10^{-5}
Helium	4	7.41×10^{-6}

Table 5: Assumed residual gas composition, based on standard atmospheric contributions, 50% relative humidity at 20 °C and 70% relative pumping speed for Helium (relative to Nitrogen).

unnecessarily massive, but the geometry allowed for simple analytical modelling because the probe volume is in that case much smaller than the cleaned volume. We approximated the void as sphere with radius R_{clean} , inscribed into the cleaned cylinder. Such minimal void will yield a quicker re-population than the actual one, and the result will be an upper limit for the number of particles to expect at a given time. In that case, symmetry can be employed to calculate, based on a Maxwellian velocity distribution, the probability that particles from the residual gas outside the spherical void can have reached the center.

The volume of interest, given by measures of relative peak intensity of the QED beam, is $\pi R_{\text{probe}}^2 \cdot L_{\text{probe}}^2 \approx 400 \mu\text{m}^3$. With the average particle density at $p = 10^{-6}$ mbar (cf. Eq. 11), the number of gas particles without cleaning is $N \approx 10$. Even with an F/1 focusing, reducing the volume by a factor $2^4 = 16$, about 1 particle would be present per shot.

Figure 14 shows how this number evolves over time, resolved by species. Until $\tau \approx 14$ ns, species evacuation takes place. It should be noted that the heavier species, despite much less abundant, set here a limit in time. This time is also an upper limit since calculations were done for single-charged molecule ions, whereas in reality, most ions will be atomic and or multiple-charged, thus evacuated quicker.

At later times, atoms from the residual gas, outside the void, can reach the probe volume. Here, Helium is important since it is the fastest species considered here, even though its contribution is very small.

For experiments is the gap from 15 ns to 25 ns important. In that time window, the expectation value of particle count means that within 10^6 shots less than one shot with a particle in the QED focus can be expected. At laser pulse repetition rates of 10 Hz, this occurrence is equivalent to less than 1 false event per 24 hours. The lowest expectation value for that simulation case amounts to $<10^{-11}$ particles at $\tau = 14.2$ ns – 14.8 ns.

For experimental realization, that time delay requires 4.5 m optical path difference. That length does not affect the

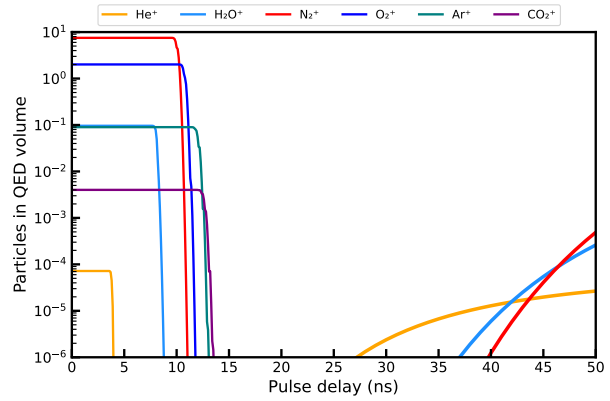


Figure 14: Simulated time dependence of lowest-Z ions and residual gas particles, counted within the probing volume, $R_{\text{probe}} = 2 \mu\text{m}$ and $L_{\text{probe}} = 32 \mu\text{m}$, for a backing pressure of $p = 10^{-6}$ mbar. The same external electric field strength as before, 2 kV over 4 mm electrode distance, yielding 0.5 MV/m is employed. Thin lines are for ions, thick lines for uncharged gas particles.

beam propagation (shorter than the beam Rayleigh length). Due to the square-root-scaling with accelerating electric field (cf. Eq. 1), the delays can be reduced by higher field strengths. A factor 10 increase of field strength to 5 MV/m would still be well below electrical breakdown thresholds and shorten delay times and optical paths by more than a factor 3 to ≈ 1.5 m, being a bearable size in a typical experimental vacuum chamber.

Prospective studies of laser-based QED experiments^[9,11,33–36] often provide the expected number of signal photons per shot for ideal conditions ($10^{-4} - 10^{-1}$ photons per shot) without consideration of background signals or fluctuating overlap conditions. Overall shot number estimates are rarely provided but are of the order of $10^5 - 10^6$ shots in total for successful measurements. Therefore, our prediction of the generation of a perfect vacuum, better than 10^6 shots without a particle in a well-defined volume of $1000 \mu\text{m}^3$ and for several 10 ns is largely sufficient. Furthermore, the apparatus allows for *in-situ* QED drive laser electric peak field characterization when the cleaning pulse is blocked and an appropriate gas like Xe is added in low concentration^[13].

Acknowledgement

The authors would like to thank Marco Garten for the ADK model ionization code^[28] and thank Lingen Huang for fruitful discussions. The authors also would like to thank the China Scholarship Council for financial support during a visit of Qiqi Yu (File No. 201908310159) to Helmholtz-Zentrum Dresden-Rossendorf and the National Natural Science Foundation of China (Grant No.11935008).

References

1. Donna Strickland and Gerard Mourou. Compression of amplified chirped optical pulses. *Optics Communications*, 56(3):219–221, 1985.
2. Colin Danson, David Hillier, Nicholas Hopps, and David Neely. Petawatt class lasers worldwide. *High Power Laser Science and Engineering*, 3:e3, 2015.
3. Colin N. Danson, Constantin Haefner, Jake Bromage, Thomas Butcher, Jean-Christophe F. Chanteloup, Enam A. Chowdhury, Almantas Galvanauskas, Leonida A. Gizzi, Joachim Hein, David I. Hillier, and et al. Petawatt and exawatt class lasers worldwide. *High Power Laser Science and Engineering*, 7:e54, 2019.
4. Christophe Radier, Olivier Chalus, Mathilde Charbonneau, Shanjuhan Thambirajah, Guillaume Deschamps, Stephane David, Julien Barbe, Eric Etter, Guillaume Matras, Sandrine Ricaud, and et al. 10 PW peak power femtosecond laser pulses at ELI-NP. *High Power Laser Science and Engineering*, 10:e21, 2022.
5. A. Di Piazza, C. Müller, K. Z. Hatsagortsyan, and C. H. Keitel. Extremely high-intensity laser interactions with fundamental quantum systems. *Reviews of Modern Physics*, 84(3):1177–1228, 2012.
6. Thomas Heinzl, Ben Liesfeld, Kay-Uwe Amthor, Heinrich Schworer, Roland Sauerbrey, and Andreas Wipf. On the observation of vacuum birefringence. *Optics Communications*, 267(2):318–321, November 2006.
7. H. Gies. Strong laser fields as a probe for fundamental physics. *The European Physical Journal D*, 55(2):311–317, 2009.
8. M. Marklund and J. Lundin. Quantum vacuum experiments using high intensity lasers. *The European Physical Journal D*, 55(2):319–326, June 2009.
9. Hans-Peter Schlenvoigt, Tom Heinzl, Ulrich Schramm, Thomas E Cowan, and Roland Sauerbrey. Detecting vacuum birefringence with x-ray free electron lasers and high-power optical lasers: a feasibility study. *Physica Scripta*, 91(2):023010, January 2016.
10. N. Ahmadiyaz, T.E. Cowan, R. Sauerbrey, U. Schramm, H.-P. Schlenvoigt, and R. Schützhold. Heisenberg limit for detecting vacuum birefringence. *Physical Review D*, 101(11), June 2020.
11. Felix Karbstein. Probing vacuum polarization effects with high-intensity lasers. *Particles*, 3(1):39–61, January 2020.
12. Lieselotte Obst-Huebl, Tim Ziegler, Florian-Emanuel Brack, João Branco, Michael Bussmann, Thomas E Cowan, Chandra B Curry, Frederico Fiuza, Marco Garten, Maxence Gauthier, Sebastian Göde, Siegfried H Glenzer, Axel Huebl, Arie Irman, Jongjin B Kim, Thomas Kluge, Stephan D Kraft, Florian Kroll, Josefine Metzkes-Ng, Richard Pausch, Irene Prencipe, Martin Rehwald, Christian Roedel, Hans-Peter Schlenvoigt, Ulrich Schramm, and Karl Zeil. All-optical structuring of laser-driven proton beam profiles. *Nature Communications*, 9(1):5292, 2018.
13. I. Ouatu, B. T. Spiers, R. Aboushelbaya, Q. Feng, M. W. Von Der Leyen, R. W. Paddock, R. Timmis, C. Ticos, K. M. Krushelnick, and P. A. Norreys. Ionization states for the multipetawatt laser-QED regime. *Physical Review E*, 106(1):1–10, 2022.
14. M. F. Ciappina, S. V. Popruzhenko, S. V. Bulanov, T. Ditmire, G. Korn, and S. Weber. Progress toward atomic diagnostics of ultrahigh laser intensities. *Physical Review A*, 99(4), April 2019.
15. M. F. Ciappina and S. V. Popruzhenko. Diagnostics of ultra-intense laser pulses using tunneling ionization. *Laser Physics Letters*, 17(2), 2020.
16. M. F. Ciappina, E. E. Peganov, and S. V. Popruzhenko. Focal-shape effects on the efficiency of the tunnel-ionization probe for extreme laser intensities. *Matter and Radiation at Extremes*, 5(4), 2020.
17. A. Yandow, T. Toncian, and T. Ditmire. Direct laser ion acceleration and above-threshold ionization at intensities from 1021 W/cm² to 3×10²³ W/cm² Direct Laser Ion Acceleration and ... A. Yandow, T. Toncian, and T. Ditmire. *Physical Review A*, 100(5):1–9, 2019.
18. O. E. Vais, A. G.R. Thomas, A. M. Maksimchuk, K. Krushelnick, and V. Yu Bychenkov. Characterizing extreme laser intensities by ponderomotive acceleration of protons from rarified gas. *New Journal of Physics*, 22(2), 2020.
19. O. E. Vais and V. Yu Bychenkov. Complementary diagnostics of high-intensity femtosecond laser pulses via vacuum acceleration of protons and electrons. *Plasma Physics and Controlled Fusion*, 63(1), 2020.
20. Anthony Link, Enam A. Chowdhury, John T. Morrison, Vladimir M. Ovchinnikov, Dustin Offermann, Linn Van Woerkom, Richard R. Freeman, John Pasley, Erik Shipton, Farhat Beg, Patrick Rambo, Jens Schwarz, Matthias Geissel, Aaron Edens, and John L. Porter. Development of an in situ peak intensity measurement method for ultraintense single shot laser-plasma experiments at the Sandia Z petawatt facility. *Review of Scientific Instruments*, 77(10), 2006.
21. K A Ivanov, I N Tsymbalov, O E Vais, S G Bochkarev, R V Volkov, V Yu Bychenkov, and A B Savel'ev. Accelerated electrons for in situ peak intensity monitoring of tightly focused femtosecond laser radiation at high intensities. *Plasma Physics and Controlled Fusion*, 60(10):105011, sep 2018.
22. A. Longman, S. Ravichandran, L. Manzo, C. Z. He, R. Lera, N. McLane, M. Huault, G. Tiscareno, D. Hanggi, P. Spingola, N. Czaplá, R. L. Daskalova, L. Roso, R. Fedosejevs, and III Hill, W. T. Toward direct spatial and intensity characterization of ultra-high-intensity laser pulses using ponderomotive scattering of

- free electrons. *Physics of Plasmas*, 30(8):082110, 08 2023.
23. Szu-yuan Chen, Anatoly Maksimchuk, and Donald Umstadter. Experimental observation of relativistic nonlinear Thomson scattering. *Nature*, 396(6712):653–655, 1998.
 24. C. Z. He, A. Longman, J. A. Pérez-Hernández, M. de Marco, C. Salgado, G. Zeraoui, G. Gatti, L. Roso, R. Fedosejevs, and W. T. Hill. Towards an in situ, full-power gauge of the focal-volume intensity of petawatt-class lasers. *Opt. Express*, 27(21):30020–30030, Oct 2019.
 25. Omri Har-Shemesh and Antonino Di Piazza. Peak intensity measurement of relativistic lasers via nonlinear thomson scattering. *Opt. Lett.*, 37(8):1352–1354, Apr 2012.
 26. Felix Mackenroth, Amol R Holkundkar, and Hans-Peter Schlenvoigt. Ultra-intense laser pulse characterization using ponderomotive electron scattering. *New Journal of Physics*, 21(12):123028, dec 2019.
 27. I. A. Aleksandrov and A. A. Andreev. Pair production seeded by electrons in noble gases as a method for laser intensity diagnostics. *Phys. Rev. A*, 104:052801, Nov 2021.
 28. Marco Garten. *Modellierung und Validierung von Feldionisation in parallelen Particle-in-Cell-Codes*. PhD thesis, Technische Universität Dresden, December 2016.
 29. Maxim V Ammosov, Nikolai B Delone, and Vladimir P Krainov. Tunnel Ionization Of Complex Atoms And Atomic Ions In Electromagnetic Field. In John A. Alcock, editor, *High Intensity Laser Processes*, volume 0664, pages 138 – 141. International Society for Optics and Photonics, SPIE, 1986.
 30. N B Delone and Vladimir P Krainov. Tunneling and barrier-suppression ionization of atoms and ions in a laser radiation field. *Physics-Uspokhi*, 41(5):469–485, May 1998.
 31. Heiko Burau, René Widera, Wolfgang Hönig, Guido Juckeland, Alexander Debus, Thomas Kluge, Ulrich Schramm, Tomas E. Cowan, Roland Sauerbrey, and Michael Bussmann. PIconGPU: A Fully Relativistic Particle-in-Cell Code for a GPU Cluster. *IEEE Transactions on Plasma Science*, 38(10):2831–2839, 2010.
 32. A. Kramida, Yu. Ralchenko, J. Reader, and NIST ASD Team. NIST Atomic Spectra Database (version 5.10). online.
 33. Baifei Shen, Zhigang Bu, Jiancai Xu, Tongjun Xu, Liangliang Ji, Ruxin Li, and Zhizhan Xu. Exploring vacuum birefringence based on a 100 pw laser and an x-ray free electron laser beam. *Plasma Physics and Controlled Fusion*, 60(4):044002, feb 2018.
 34. Elena A. Mosman and Felix Karbstein. Vacuum birefringence and diffraction at an x-ray free-electron laser: From analytical estimates to optimal parameters. *Physical Review D*, 104(1):13006, 2021.
 35. Qiqi Yu, Dirui Xu, Baifei Shen, Thomas E. Cowan, and Hans-Peter Schlenvoigt. X-ray polarimetry and its application to strong-field quantum electrodynamics. *High Power Laser Science and Engineering*, 11:e71, 2023.
 36. N. Ahmadinia, C. Bähz, A. Benediktovitch, C. Bömer, L. Bocklage, T. E. Cowan, J. Edwards, S. Evans, S. Franchino Viñas, H. Gies, S. Göde, J. Görs, J. Grenzer, U. Hernandez Acosta, T. Heinzl, P. Hilz, W. Hippler, L. G. Huang, O. Humphries, F. Karbstein, P. Khademi, B. King, T. Kluge, C. Kohlfürst, D. Krebs, A. Laso-García, R. Löttsch, A. J. Macleod, B. Marx-Glowna, E. A. Mosman, M. Nakatsutsumi, G. G. Paulus, S. V. Rahul, L. Randolph, R. Röhlberger, N. Rohringer, A. Sävert, S. Sadashivaiah, R. Sauerbrey, H.-P. Schlenvoigt, S. M. Schmidt, U. Schramm, R. Schützhold, J. P. Schwinkendorf, D. Seipt, M. Šmíd, T. Stöhlker, T. Toncian, M. Valialshchikov, A. Wipf, U. Zastra, and M. Zepf. Letter of Intent: Towards a Vacuum Birefringence Experiment at the Helmholtz International Beamline for Extreme Fields. <https://arxiv.org/abs/2405.18063>, accepted for publication at High Power Laser Science and Engineering, 2024.